J. Fluid Mech. (1998), *vol.* 369, *pp.* 333–350. Printed in the United Kingdom

Band structure of surface flexural–gravity waves along periodic interfaces

By TOM CHOU

Department of Applied Mathematics and Theoretical Physics, University of Cambridge, Silver Street, Cambridge CB3 9EW, UK

(Received 7 March 1997 and in revised form 8 April 1998)

We extend Floquet's Theorem, similar to that used in calculating electronic and optical band gaps in solid state physics (Bloch's Theorem), to derive dispersion relations for small-amplitude water wave propagation in the presence of an infinite array of periodically arranged surface scatterers. For one-dimensional periodicity (stripes), we find band gaps for wavevectors in the direction of periodicity corresponding to frequency ranges which support only non-propagating standing waves, as a consequence of multiple Bragg scattering. The dependence of these gaps on scatterer strength, density, and water depth is analysed. In contrast to band gap behaviour in electronic, photonic, and acoustic systems, we find that the gaps here can increase with excitation frequency ω. Thus, higher-order Bragg scattering can play an important role in suppressing wave propagation. In simple two-dimensional periodic geometries no complete band gaps are found, implying that there are always certain directions which support propagating waves. Evanescent modes offer one qualitative reason for this finding.

1. Introduction

Scattering of monochromatic acoustic, electromagnetic, or electronic wave functions is described by the Helmholtz equation, a boundary condition at the scatterer interface, and a radiation condition far away from the body. These conditions uniquely solve most scattering problems. Although surface perturbations on an ideal fluid propagate as waves, and general principles of scattering theory from other contexts apply, the incompressibility condition in the bulk liquid has no spatial variation. Thus, scattering can occur only through interactions with localized geometrical variation of the boundaries, or localized variations in the conditions imposed at the boundaries. An example of the former is the scattering of water waves from variations in bottom depth studied by Mei (1985), Belzons, Guazzelli & Parodi (1988), Davies, Guazzelli & Belzons (1989) and Mitra & Greenberg (1984), which has implications for design of underwater breakwaters (Mei, Hara & Naciri 1988), long distance ocean wave propagation (Elter & Molyneaux 1972), wave propagation over rippled beds near beaches (Mei 1985; Naciri & Mei 1988; Davies *et al.* 1989 and Kirby 1986), and thirdly sound propagation of superfluid helium films as discussed by Kleinert (1990). Periodic bottom depths, or periodically arranged impenetrable obstacles piercing the sea surface, have also been studied theoretically with multiple scattering analyses by Mei (1983), Kagemoto & Yue (1986) and Porter & Evans (1995). Integral equation techniques have been applied to periodic breakwaters by Fernyhough & Evans (1995) and to bottom depths by Black, Mei & Bray (1971).

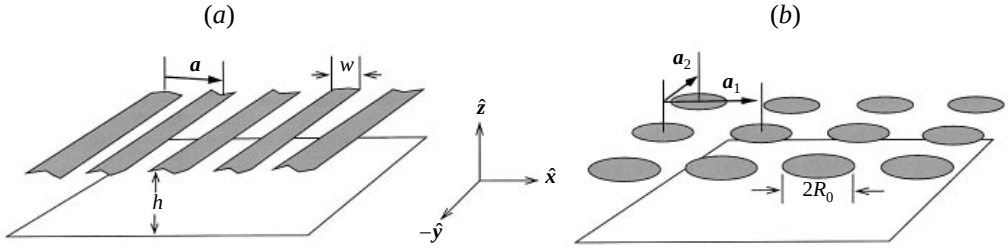

FIGURE 1. Schematic of periodic scatterers at the liquid interface. The depth is a constant h, and the bending rigidity and/or surface tension is D_2 and/or σ_2 inside the shaded regions and D_1 and/or σ_1 outside. Depicted here are scatterers which have sharp discontinuities in D and σ along the surface, in (a) one-dimensional stripes of width w, and (b) square array of disks of radius R_0.

In these studies the possibility of resonant Bragg scattering from finite structural arrays was recognized by Mei (1983), Davies *et al.* (1989) and Mitra & Greenberg (1984); however, only first-order Bragg scattering has been discussed. Random bottoms has also been studied using shallow water theory, where interesting localization behaviour has been theoretically predicted and experimentally observed by Devillard, Dunlop & Souillard (1988), and Belzons *et al.* (1988) and Elter & Molyneaux (1972), respectively.

In this paper we consider the scattering that occurs when surface constitutive parameters, such as surface tension or surface bending rigidity in the boundary conditions are spatially varying along the interface. Lucassen-Reynders & Lucassen (1969) show that surfactant deposition at the air–water interface drastically attenuates wave propagation, and multiple surface wave scattering from surfactant concentration variations has been suggested by Chou & Nelson (1994) as one contributing mechanism. Monolayers of surfactants at air–water interfaces can phase separate into periodic domains as a consequence of line tension and microscopic dipolar interactions (Andelman, Brochard & Joanny 1987 and Knobler & Desai 1992). Similarly, ice floes, which vary the surface mass density as well as surface bending moments at the air–sea interface, also scatter water waves and attenuate wave energy in Marginal Ice Zones (MIZ) (Fox & Squire 1990 and Squire *et al.* 1995). Here, regular patterns of surface ice thickness can form due to periodic convection of freezing surface waters, or current instabilities of a freezing mushy ice zone. Also, stress from incident water waves on an ice sheet can break strips of ice off the leading edge and form very long, regular stripes of ice separated by open sea (Squire *et al.* 1995). An approximate two-dimensional periodicity also exists in regions of pancake ice, where circular floes occupy a high filling fraction of the surface. All of the physical systems mentioned are schematically depicted in figure 1 in the limit of perfect periodicity.

Reflection and transmission coefficients of water wave scattering from semi-infinite flexible docks have been calculated using variational methods and numerical solution of integral equations by Squire *et al.* (1995), Liu & Mollo-Christensen (1988), and Meylan & Squire (1994); however, only the amplitudes have been explicitly calculated. When considering multiple scattering, however, the phase is a critical variable to be considered as it affects whether waves interfere constructively or destructively. An integral equation solution to the reflection and transmission coefficients of scattering from a semi-infinite surface tension discontinuity has been found by Gou, Messiter & Schulze (1993), but the energy conservation was applied *a posteori* and phase shifts were not found.

Irrespective of the numerous treatments of water wave scattering, we show here that an exact solution to the dispersion relation of surface waves propagating in an *infinite periodic* array of surface scatterers (such as ice floes) can be simply calculated. The results represent the effects of multiple scattering and allow easy physical interpretation.

In the following Section we formulate the model describing surface wave propagation in the presence of an infinite periodic array of surface deformable scatterers (figure 1). We adapt a technique (Floquet's Theorem) often used in solid state physics, to study multiple surface wave scattering. An analogous 'phase ansatz' was used by Fernyhough & Evans (1995) and Porter & Evans (1995) to study surface wave scattering from rectangular breakwaters. In our problem, the surface boundary conditions are spatially periodic and are cast into a matrix equation with eigenvalues which determine wave dispersion.

In § 3, we consider both one- and two-dimensional arrays of surface scatterers (see figure 1). The physical features of the dispersion relations are displayed and qualitatively explained. We find stop bands, or band gaps, analogous to those found in other systems (Ashcroft & Mermin 1976; McCall *et al.* 1991; Sigalas & Economu 1992), where as a consequence of the coupling between the periodic nature of the scatterers and the plane-wave-decomposed velocity field, the dispersion relation $\omega(k)$ has jumps between which the excitation frequencies do not correspond to extended plane waves, but rather localized, standing waves. The wavevectors where these frequency jumps occur define 'Bragg' points (one-dimension) or lines (two-dimension) in Fourier space where resonant multiple scattering interferes in such a way that waves do not propagate. Rather than provide an exhaustive array of numerical calculations, we emphasize the physical phenomena of band gaps and their dependence on parameters such as scattering strength, water depth, and surface scatterer filling fraction.

In § 4, we mention the general features of the basic results and their implications for multiple scattering in natural and manmade applications, such as wave propagation in ice fields and arrays of surface plates. In the Appendix, we generalize Floquet theory or Bloch's Theorem to include dynamics governed by periodic boundary conditions.

2. Model of periodic surface waves

The dynamics of an interface overlying an ideal fluid of depth h (figure 1) is derived by balancing surface stresses and deriving dynamical equations which govern surface wave propagation. The analyses are restricted to *surface* scatterers; structures are assumed to have small thicknesses d ($d \ll \lambda, h$, where λ is any wavelength), lie entirely at the interface $z \simeq 0$, and do not change the domain over which Laplace's equation for the velocity potential holds. Examples are thin plates with bending stiffness or domains of surface-active materials which locally decrease surface tension. The scatterers are periodic and their in-plane interfacial positions are assumed fixed.

2.1. *Surface water waves*

The motion of the interface is coupled to the bulk flow which is described by the Euler equation for incompressible ideal flows,

$$\partial_t \boldsymbol{v} + (\boldsymbol{v} \cdot \nabla)\boldsymbol{v} = -\frac{1}{\rho}\nabla p + \rho \boldsymbol{g}, \qquad z < \eta(\boldsymbol{r}, t), \tag{2.1}$$

where ρ is the bulk fluid density, $\rho \boldsymbol{g} \equiv -\rho g \hat{\boldsymbol{z}}$ is the external body force density due to gravity, p is the dynamic pressure, and $\eta(\boldsymbol{r}, t)$ is the surface deformation as a function of surface coordinate $\boldsymbol{r} \equiv (x, y)$. We neglect all dynamical effects of the upper fluid, air. By assuming irrotational flows, the velocity is potential, $\boldsymbol{v} \equiv \nabla\varphi$. Hence,

$$\nabla \cdot \boldsymbol{v} = \nabla^2 \varphi(\boldsymbol{r}, z, t) = (\nabla_\perp^2 + \partial_z^2)\varphi(\boldsymbol{r}, z, t) = 0, \qquad z < \eta(\boldsymbol{r}), \tag{2.2}$$

where $\nabla_\perp^2 \equiv \partial_x^2 + \partial_y^2$ is the two-dimensional Laplacian in the coordinates of figure 1. The linearized kinematic conditions at the free interface and the impenetrable bottom ($\hat{\boldsymbol{z}} \cdot \boldsymbol{v}(z = -h) = 0$) are

$$\lim_{z \to 0^-} \partial_z \varphi(\boldsymbol{r}, z, t) = \partial_t \eta \tag{2.3}$$

and

$$\lim_{z \to -h^+} \partial_z \varphi(\boldsymbol{r}, z, t) = 0, \tag{2.4}$$

respectively. The linearized normal fluid stress at the interface is

$$P_{nn} \equiv \lim_{z \to 0^-} \rho \left[\partial_t \varphi + g\eta(\boldsymbol{r}, t)\right] \simeq P_{zz}, \tag{2.5}$$

where we have assumed the absence of externally imposed stream flow and that the only disturbances are in the form of dynamic surface waves. The fluid stress P_{nn} is balanced by material restoring forces such as those due to surface bending and stretching. In the absence of fluid viscous stresses, the application of surface stresses must be carefully applied to ensure conservation of $\hat{\boldsymbol{z}}$-component forces, torques, and bending moments. These forces and the energy are manifestly conserved when the surface stresses are derived from an energy functional for the bulk fluid plus interface. For example, P_{zz} and gradients of $\sigma(\boldsymbol{r})$ have to be considered in inviscid fluids to conserve wave energy. Thus, the net $\hat{\boldsymbol{z}}$-component surface stress balance reads

$$\left[\nabla_\perp \cdot (\sigma(\boldsymbol{r})\nabla_\perp) - \nabla_\perp^2 (D(\boldsymbol{r})\nabla_\perp^2)\right] \eta(\boldsymbol{r}, t) = P_{zz} \tag{2.6}$$

which upon taking the time derivative and using (2.3) becomes

$$\lim_{z \to 0^-} \left[\nabla_\perp \cdot (\sigma(\boldsymbol{r})\nabla_\perp) - \nabla_\perp^2 (D(\boldsymbol{r})\nabla_\perp^2)\right] \partial_z \varphi(\boldsymbol{r}, z, t) = \partial_t P_{zz}, \tag{2.7}$$

where $D(\boldsymbol{r})$ and $\sigma(\boldsymbol{r})$ are the surface flexural rigidity and surface tension respectively. In (2.7), we have neglected the rotational inertial terms in the surface bending stresses, valid when $\omega^2 \ll E\rho_s^{-1}/\lambda^2$ (ρ_s is the bulk mass density of the surface material). Within thin plate theory, $D = Ed^3/12(1 - s^2)$ where E and s are Young's modulus and Poisson's ratio of the surface material in its bulk phase.

Consider dynamical variables with a time dependence of the form $\mathrm{e}^{-\mathrm{i}\omega t}$. In the frequency domain, we combine the time derivative of the $\hat{\boldsymbol{z}}$-component stresses and use (2.3) and (2.5) to obtain

$$\begin{aligned} \lim_{z \to 0^-} \left[\rho\omega^2 \varphi(\boldsymbol{r}, z) - \left(\rho g - \nabla_\perp \cdot (\sigma(\boldsymbol{r})\nabla_\perp) + \nabla_\perp^2 (D(\boldsymbol{r})\nabla_\perp^2)\right) \partial_z \varphi(\boldsymbol{r}, z)\right] \\ \equiv \left[\rho\omega^2 \lim_{z \to 0^-} -\mathbf{L}(\boldsymbol{r}, \omega)\right] \varphi(\boldsymbol{r}, z) = 0. \end{aligned} \tag{2.8}$$

Equations (2.8) and (2.2) determine the velocity potential with frequency ω. The effects of spatially varying surface properties are implicit in the boundary condition (2.8). In the limit of uniform $\sigma(\boldsymbol{r}) = \sigma$ and $D(\boldsymbol{r}, t) = D$, $\varphi \propto \mathrm{e}^{\pm \mathrm{i}\boldsymbol{k}\cdot\boldsymbol{r}} \cosh k(h + z)$, from which we obtain the standard gravity–capillary–flexural wave dispersion relation

$$\omega^2 = \left(gk + \frac{\sigma}{\rho}k^3 + \frac{D}{\rho}k^5\right) \tanh kh, \tag{2.9}$$

where $k = |\boldsymbol{k}| = 2\pi/\lambda$. This relation is valid only for uniform surfaces or very far (many wavelengths) from localized spatial inhomogeneities of the surface parameters $\sigma(\boldsymbol{r})$ and $D(\boldsymbol{r})$.

However, when σ and/or D are not uniform, surface waves can diffract or refract from the regions of varying surface properties and the Fourier modes of the velocity potential at the interface mix with those of the surface variations. The remainder of this study deals with periodic variations in $\sigma(\boldsymbol{r})$ and $D(\boldsymbol{r})$ where the boundary condition (2.8) is to be used to solve $\nabla^2\varphi(z < 0) = 0$. Since the effects we will consider arise from multiple scattering of the surface waves, we require for real fluids a viscous dissipation length

$$k_d^{-1} \sim \min\left[\frac{g^3}{\nu\omega^5}, \frac{\sigma}{\rho\nu\omega}, \frac{1}{\nu}\left(\frac{D^3}{\rho^3\omega}\right)^{1/5}\right] \gg a, \tag{2.10}$$

where ν is the kinematic viscosity, and σ, D above are their minimum values along the periodic interface. We have assumed (2.10) holds by treating ideal fluids. Although our treatment is linear in small surface displacements, there are no constraints on the periodic spatial variations of D, σ and scattering can be strong.

2.2. *Bloch functions and periodic solutions*

The following analysis is similar to the treatment of a single particle electronic wave function in a periodic potential. Further details are given in Chapters 5 and 8 of Ashcroft & Mermin (1976). Joannopoulos, Meade & Winn (1995) also consider light propagation through a medium with periodic inclusions of different dielectric constants. These references describe in detail the terminology used; however, our surface scattering problem is sufficiently different that we will give a largely complete formulation below. Near (within a few wavelengths) sources or variations in σ or D, the velocity potential cannot be represented by a single wavevector component and must be decomposed into a complete set of plane wave eigenfunctions. For example, the choice

$$\varphi(\boldsymbol{r}, z) = \sum_{\boldsymbol{k}} \varphi_{\boldsymbol{k}}\, \mathrm{e}^{\mathrm{i}\boldsymbol{k}\cdot\boldsymbol{r}}\, \frac{\cosh k(h+z)}{\cosh kh} \tag{2.11}$$

manifestly satisfies Laplace's equation and (2.4). For the surface scatterers, we consider one- and two-dimensional periodicities, with lattice vectors $\boldsymbol{a}$ (see figure 1). Since the surface properties are periodic in $\boldsymbol{a}_i$,

$$D(\boldsymbol{r} + n_i\boldsymbol{a}_i) = D(\boldsymbol{r}), \tag{2.12}$$

where n_i are integers and index summation convention is used. Thus, the Fourier decomposition of $\sigma(\boldsymbol{r})$, $D(\boldsymbol{r})$ can be written in the form

$$\sigma(\boldsymbol{r}) = \sum_{m,n} \sigma(\boldsymbol{G})\mathrm{e}^{\mathrm{i}\boldsymbol{G}\cdot\boldsymbol{r}}, \quad D(\boldsymbol{r}) = \sum_{m,n} D(\boldsymbol{G})\mathrm{e}^{\mathrm{i}\boldsymbol{G}\cdot\boldsymbol{r}}, \tag{2.13}$$

where $\boldsymbol{G}$ are the corresponding reciprocal lattice vectors for stripe, square, and triangular lattices with periodicity a,

$$\left.\begin{aligned} \boldsymbol{G}(m) &= \frac{2\pi m}{a}\hat{\boldsymbol{x}} \equiv m\boldsymbol{G}(1) && \text{(stripes)},\\ \boldsymbol{G}(m,n) &= \frac{2\pi m}{a}\hat{\boldsymbol{x}} + \frac{2\pi n}{a}\hat{\boldsymbol{y}} && \text{(square)},\\ \boldsymbol{G}(m,n) &= \frac{4\pi m}{\sqrt{3}a}\hat{\boldsymbol{x}} + \frac{2\pi n}{\sqrt{3}a}(\hat{\boldsymbol{x}} - \sqrt{3}\hat{\boldsymbol{y}}) && \text{(triangular)}, \end{aligned}\right\} \tag{2.14}$$

with m, n integers. The Fourier decomposition of $\sigma(\boldsymbol{r})$ and $D(\boldsymbol{r})$ are completely represented by these sets of wavevectors. Furthermore, since the set $\{\boldsymbol{G}\}$ also forms a periodic lattice in wavevector space, any particular reciprocal lattice vector in the set $\{\boldsymbol{G}\}$ for each type of lattice can be constructed by a countable number of others within that set. In fact, the lattice in wavevector space has the same symmetry properties as the real space lattice defined by $\sigma(\boldsymbol{r})$, $D(\boldsymbol{r})$. We exploit the periodicity of $D(\boldsymbol{r})$ in the boundary condition (2.8) and use Bloch's theorem (a multidimensional generalization of Floquet's Theorem), to find another representation related to (2.11).

Floquet's Theorem (or the multidimensional generalization, Bloch's Theorem) states that a solution to a linear differential equation with periodic coefficients can be represented as a product of a phase factor and another function which is invariant under the periodicity of the coefficients (Mathews & Walker 1970):

$$\varphi(\boldsymbol{r}, z) \equiv \mathrm{e}^{-\mathrm{i}\boldsymbol{q}\cdot\boldsymbol{r}}\phi(\boldsymbol{r}, z) = \mathrm{e}^{-\mathrm{i}\boldsymbol{q}\cdot\boldsymbol{r}} \sum_{\boldsymbol{G}} \phi_{\boldsymbol{q}}(\boldsymbol{G})\mathrm{e}^{\mathrm{i}\boldsymbol{G}\cdot\boldsymbol{r}} \frac{\cosh|\boldsymbol{q}-\boldsymbol{G}|(h+z)}{\cosh|\boldsymbol{q}-\boldsymbol{G}|h} \tag{2.15}$$

where $\boldsymbol{q}$ is the phase parameter to be related to $\boldsymbol{k}$, the physical wavevector. The last equality arises from expanding the periodic function $\phi(\boldsymbol{r} + n_i\boldsymbol{a}_i) \equiv \phi(\boldsymbol{r})$ in a manner identical to $D(\boldsymbol{r})$ or $\sigma(\boldsymbol{r})$. Although the periodicity in this problem resides in the operator $\mathbf{L}(\boldsymbol{r}, z, \omega)$ and not in $\nabla^2\varphi = 0$, we explicitly demonstrate the validity of Bloch's Theorem and (2.15) in the Appendix.

Now consider a large array of scatterers that are periodically repeated to construct an infinite system. Application of periodic boundary conditions on the entire array of scatterers (Born–von Kármán boundary conditions) requires

$$\varphi(\boldsymbol{r}, z) = \varphi(\boldsymbol{r} + N_i\boldsymbol{a}_i, z), \tag{2.16}$$

where N_i is the total number of scatterers in the i-direction (such that $N_i a$ is the system size in the i-direction) which is repeated in the periodic scheme. Upon substitution of (2.15) into (2.16), $\boldsymbol{q}$ is restricted to the real values

$$\boldsymbol{q}\cdot\boldsymbol{a}_i = \frac{2\pi n}{N_i}. \tag{2.17}$$

Thus, the granularity of $\boldsymbol{q}$ is determined by the total number of scatterers. Since by construction $a|\boldsymbol{G}(1)| = 2\pi$ in one dimension and $\boldsymbol{a}_1\cdot\boldsymbol{G}(1,0) = \boldsymbol{a}_2\cdot\boldsymbol{G}(0,1) = 2\pi$ in two dimensions, the values of $\boldsymbol{q}$ are defined by

$$\left.\begin{aligned} \boldsymbol{q} &= \frac{n}{N}\boldsymbol{G}(1), && \text{1D Periodicity},\\ \boldsymbol{q} &= \frac{n_1}{N_1}\boldsymbol{G}(1,0) + \frac{n_2}{N_2}\boldsymbol{G}(0,1), && \text{2D Periodicity}. \end{aligned}\right\} \tag{2.18}$$

If we choose the values of n, n_1, n_2 such that $n \in [-N/2, N/2]$, $n_i \in [-N_i/2, N_i/2]$, the maximal values of the 'reduced wavevector' $|\boldsymbol{q}|$ in the $(0,1)$ and $(1,0)$ directions

are $|\boldsymbol{G}(0,1)|/2$ and $|\boldsymbol{G}(1,0)|/2$, respectively. This region of $\boldsymbol{q}$-space defines the first Brillouin Zone (BZ). For example, in one dimension, this first zone is specified by $q_x \in [-\pi/a, \pi/a]$. Comparison of (2.11) and (2.15) shows that the physical wavevectors $\boldsymbol{k}$ are represented by $\boldsymbol{q}$, with very short wavelengths described by $\boldsymbol{q}$ with added multiples of $\boldsymbol{G}$.

Direct substitution of (2.15) into (2.8) yields for each of the N (one dimension) or $N_1 N_2$ (two dimensions) values of $\boldsymbol{q}$,

$$\rho\left(\omega^2 - \Omega_{\boldsymbol{q}}^2(\boldsymbol{G})\right)\phi_{\boldsymbol{q}}(\boldsymbol{G}) = \sum_{\boldsymbol{G}' \neq \boldsymbol{G}} \Big[|\boldsymbol{q}-\boldsymbol{G}|^2 |\boldsymbol{q}-\boldsymbol{G}'|^3 D(\boldsymbol{G}-\boldsymbol{G}') + (\boldsymbol{q}-\boldsymbol{G}')\cdot(\boldsymbol{q}-\boldsymbol{G})|\boldsymbol{q}-\boldsymbol{G}'|\sigma(\boldsymbol{G}-\boldsymbol{G}')\Big] \tanh|\boldsymbol{q}-\boldsymbol{G}'|h\,\phi_{\boldsymbol{q}}(\boldsymbol{G}') \tag{2.19}$$

where

$$\Omega_{\boldsymbol{q}}^2(\boldsymbol{G}) \equiv \left(g|\boldsymbol{q}-\boldsymbol{G}| + \frac{\sigma_0}{\rho}|\boldsymbol{q}-\boldsymbol{G}|^3 + \frac{D_0}{\rho}|\boldsymbol{q}-\boldsymbol{G}|^5\right)\tanh|\boldsymbol{q}-\boldsymbol{G}|h \tag{2.20}$$

and $\sigma_0 = \sigma(\vec{0})$ and $D_0 = D(\vec{0})$ are the spatially averaged (zero wavevector) surface properties. In (2.19) have ensured $\boldsymbol{q}$ lies in the first BZ demanded by (2.18) and our choice of range of n_i by using the fact that any sum or difference of reciprocal lattice vectors yields another reciprocal lattice vector, $\boldsymbol{G}-\boldsymbol{G}' = \boldsymbol{G}''$. Since $\boldsymbol{G}' \equiv m'\boldsymbol{G}(1,0) + n'\boldsymbol{G}(0,1)$, the sum $\sum_{\boldsymbol{G}'} \equiv \sum_{m',n'}$. Equation (2.19) is the fundamental matrix equation that determines the relationship between frequency ω and reduced wavevector $\boldsymbol{q}$. Instead of having a coupled equation for all physical wavevectors, (2.19) and (2.20) couple the coefficients $\phi_{\boldsymbol{q}}(\boldsymbol{G})$, $\phi_{\boldsymbol{q}}(\boldsymbol{G}')$, $\phi_{\boldsymbol{q}}(\boldsymbol{G}'')$, …, or only the velocity potentials with wavevectors which differ by multiples of $\boldsymbol{G}$. The choice of restricting $\boldsymbol{q}$ to the first BZ by proper choice of $\boldsymbol{G}$ is the reduced-zone scheme and is useful when calculating and presenting the eigenvalues of (2.19). The set of N or $N_1 N_2$ eigenvalues ($\rho\omega^2$) will be associated with surface deformations with physical wavevectors $\boldsymbol{q}+\boldsymbol{G}$. For example, at a fixed $\boldsymbol{q}$, the first eigenvalue of (2.19) corresponds to $\boldsymbol{k} = \boldsymbol{q}$, while the next higher eigenvalue corresponds to $\boldsymbol{k} = \boldsymbol{q} + \boldsymbol{G}(1,0)$, and so on.

For the sake of clarity and simplicity, we will only consider the case where $\sigma = 0$ relevant for long flexural–gravity waves ($2\pi(\sigma/\rho g)^{1/2} \ll \lambda \ll 2\pi(D/\sigma)^{1/2}$). Thus the scattering originates only from the the periodically varying bending rigidities at the interface. The extension to include $\sigma(\boldsymbol{G}) \neq 0$ for studying surface waves in the presence of periodic surfactant coverage is straightforward. The matrix equation affords an eigenvalue spectrum corresponding to $\rho\omega^2$ for each value of $\boldsymbol{q}$. Thus, the square-root of the eigenvalues gives the dispersion relation for surface waves propagating over periodic surfaces.

The matrix (2.19) can be written in an inherently symmetric form (hence all eigenvalues are real as expected from an ideal, stable system) by considering renormalized Fourier coefficients $\phi'_{\boldsymbol{q}}(\boldsymbol{G}) = |\boldsymbol{q}-\boldsymbol{G}|\tanh|\boldsymbol{q}-\boldsymbol{G}|h\,\phi_{\boldsymbol{q}}(\boldsymbol{G})$. The problem is therefore a generalized eigenvalue problem $\boldsymbol{A}'\phi'_{\boldsymbol{q}} = \rho\omega^2\boldsymbol{B}\phi'_{\boldsymbol{q}}$ where $\boldsymbol{B}$ is diagonal. Applying the inverse of the square-root of $\boldsymbol{B}$ to both sides (Cholesky decomposition), the problem is recast into a symmetric eigenvalue problem,

$$\det|\boldsymbol{A} - \rho(\omega^2 - \Omega_{\boldsymbol{q}}^2)\boldsymbol{I}| = 0, \tag{2.21}$$

where

$$\boldsymbol{A}(\boldsymbol{G} \neq \boldsymbol{G}') = D(\boldsymbol{G}-\boldsymbol{G}')|\boldsymbol{q}-\boldsymbol{G}|^{5/2}|\boldsymbol{q}-\boldsymbol{G}'|^{5/2}\tanh^{1/2}|\boldsymbol{q}-\boldsymbol{G}|h\tanh^{1/2}|\boldsymbol{q}-\boldsymbol{G}'|h. \tag{2.22}$$

The above symmetrization facilitates the calculation and computational convergence of the eigenvalues $\rho\omega^2$ of $\boldsymbol{A} + \rho\Omega_{\boldsymbol{q}}^2\boldsymbol{I}$.

We now input specific one- and two-dimensional periodic 'surface potentials' $D(\boldsymbol{G}-\boldsymbol{G}')$. In one dimension, we consider strips of scatterers corresponding to a surface sheet with alternating bending rigidities $D(x) = D_1$ or $D(x) = D_2$ depending on whether x is inside or outside a strip, respectively (see figure 1*a*). For two-dimensional periodic surface scatterers, we consider both square (figure 1*b*) and triangular (not shown) lattices of circular disks of radius R_0. Inside each disk, $D = D_2$, while outside $D = D_1$. The Fourier transforms of the above scattering potentials are, $D(\vec{0}) = D_0 \equiv \bar{D} = (1-f)D_1 + fD_2$, and

$$\left.\begin{aligned} D(\boldsymbol{G} \neq \vec{0}) &= \frac{D_2 - D_1}{\pi|\boldsymbol{G}|}\sin(|\boldsymbol{G}|af), \qquad \text{1D periodicity,} \\ D(\boldsymbol{G} \neq \vec{0}) &= 2f\frac{(D_2 - D_1)}{|\boldsymbol{G}|R_0}J_1(|\boldsymbol{G}|R_0) \quad \text{2D periodicity,} \end{aligned}\right\} \tag{2.23}$$

where f is the fraction of area covered by the D_2 material, and $\boldsymbol{G}$ is a reciprocal lattice vector from the appropriate set in (2.14). Our choices above are numerically the most laborious due to Gibb's phenomenon at the sharp discontinuities in $D(\boldsymbol{r})$; nonetheless, we find that the eigensolutions to (2.21) converge rapidly as a function of matrix size.

3. Results and discussion

We numerically solve the eigenvalue problem represented by (2.21) and (2.22) for each $\boldsymbol{q}$ (in the $N_i \to \infty$ limit, $\boldsymbol{q}$ becomes a continuous variable) using standard methods described in Press *et al.* (1992). Typically, 256 different $\boldsymbol{G}$ (or (m, n) pairs) are taken (corresponding to a 256×256 matrix) for both the one- and two-dimensional cases, such that the lowest 4–6 eigenvalues do not change appreciably ($< 1\%$) upon halving the matrix size. The calculations converge very efficiently for the lowest 4–6 eigenvalues especially in two dimensions because the additional Bessel function J_1 makes the off-diagonal elements diminish relatively faster away from the diagonal. The matrix calculations for smoother variations in $D(\boldsymbol{r})$ are even simpler; for example, $\boldsymbol{A}$ is tridiagonal when D is sinusoidal. In our numerical plots, all distances are scaled with respect to lattice spacing, and wavevectors are measured in units of a^{-1}. The frequency is non-dimensionalized and plotted in units of $(g/a)^{1/2}$, and the bending rigidity is shown in units of $\rho g a^4/\pi^4$.

3.1. *One-dimensional periodicity*

The choice $D_1 = 0$, $D_2 \neq 0$ is appropriate for open water punctuated by flexible strips and illustrates the difference between gravity and bending waves. For concreteness, consider $D_2 = 3.0$, which for the Young's modulus and Poisson's ratio of sea ice ($E = 6 \times 10^{10}$ dynes cm^{-1} and $s = 0.3$), and periodicities of 1.0 m, corresponds to a $d \sim 0.8$ cm ice layer. At this coverage, the dispersion within the ice sheet is predominately determined by bending forces (compare the terms gq and $\bar{D}q^5/\rho$) except at large wavelengths such that $q \lesssim (\rho g/\bar{D})^{1/4}$.

The first few eigenvalues, or bands, (labelled by n) in the dispersion relation for wave propagating in an array of one-dimensional periodic surface scatterers are plotted in figure 2. Here, $h = \infty$, the filling fraction $f = 0.6$, and $D_2 = 3.0$. The right-hand panel shows the dispersion relation for $q_y = 0$ as a function of q_x, the reduced wavevector

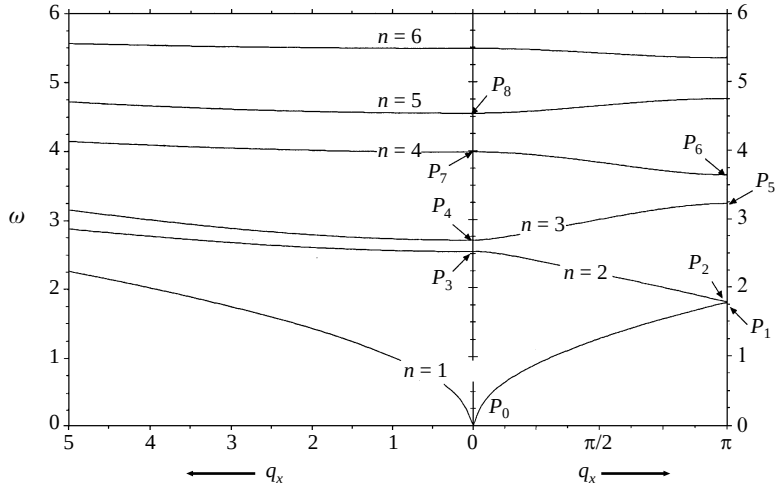

FIGURE 2. The dispersion relation, or band structure of surface waves ($h = \infty$) in the presence of discontinuous stripes of surface bending rigidity $D(x)$. Lengths are measured in units of periodicity a and frequencies are measured in units of $(g/a)^{1/2}$. Surface values used are $\sigma = 0$, $D_1 = 0$, $D_2 = 3.0$, and filling fraction $w/a \equiv f = 0.6$. The right-hand panel plots $\omega(q_x, 0)$, the left, $\omega(0, q_y)$, where $\omega(\boldsymbol{q}) = \omega(-\boldsymbol{q})$. The dispersion relation ($q_y = 0$) is plotted in the reduced-zone scheme where for example, the first ($n = 1$) eigenvalues correspond to $q_x = k_x$, $n = 2$ correspond to $k_x = |\boldsymbol{G}(1)| - q_x$, $n = 3$ to $k_x = |\boldsymbol{G}(1)| + q_x$, $n = 4$ to $2|\boldsymbol{G}(1)| - q_x$, etc. Note the first small band gap between $\omega(P_1) \simeq 1.77$ and $\omega(P_2) \simeq 1.79$. Dispersion of waves with a component in the k_y-direction are shown in the left-hand panel. Waves travelling in the $\hat{\boldsymbol{y}}$-direction are described by the $n = 1$ eigenvalues, while $n = 2, 3$ correspond to $\boldsymbol{k} = \pm q_y \hat{\boldsymbol{y}} + \boldsymbol{G}(1)$.

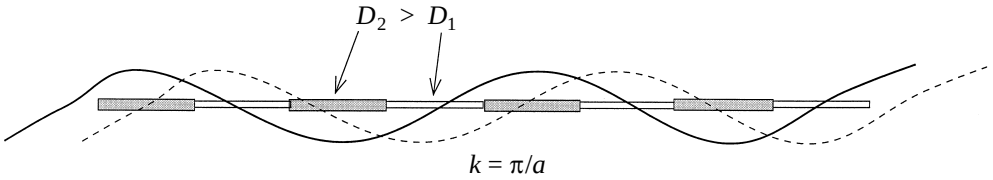

FIGURE 3. Wave configurations $(q_x, 0)$ near the wavevectors of the first gap. The solid(dotted) modes are continuous with bands terminating at $q_x = \pi/a \pm \epsilon$ or $P_1(P_2)$.

in the direction of periodicity. We have plotted the axis according to the reduced-zone scheme where the dispersion relations are folded at every half unit reciprocal lattice vector $\boldsymbol{G}(1)/2$, i.e. at $(q_x = 0, \pi)$ where Bragg scattering of surface waves occurs. The different ω found from the eigenvalues correspond to wavevectors k_x related to the plotted values of q_x shifted by appropriate multiples of reciprocal lattice vectors $\boldsymbol{G}(1)$. If $\omega(\boldsymbol{k})$ were plotted as a function of physical wavevector k_x instead, there would be one curve following $P_0 - P_1 - P_2 - P_3 - P_4 - \ldots$, as physical wavevector k_x increased. The curve in this representation would be punctuated by discontinuous jumps at certain wavevectors (multiples of $\boldsymbol{G}(1)/2$) corresponding to Bragg scattering.

The left-hand panel shows $\omega(0, q_y)$; only the lowest branch ($n = 1$) corresponds to a wave propagating in the $\hat{\boldsymbol{y}}$-direction. Interestingly, the motions corresponding to this mode have no variation in the $\hat{\boldsymbol{x}}$-direction. For the set of parameters considered, this wave has a predominantly gravity-wave-like dispersion. The higher branches $n = 2, 3$ correspond to $\boldsymbol{k} = q_y \hat{\boldsymbol{y}} + \boldsymbol{G}(1)$ and $n = 4, 5$ correspond to $\boldsymbol{k} = q_y \hat{\boldsymbol{y}} + 2\boldsymbol{G}(1)$.

The calculated gaps (such as $\omega(P_1) - \omega(P_2)$) are discontinuities in $\omega(k_x)$ and are associated with multiple Bragg scattering. Physically, oscillations with frequencies $\omega(P_1)[\omega(P_2)]$ correspond to deformations with most of the wave nodes[antinodes] located in the low-D_1 surface rigidity regions. The origin of the first gap $\omega(P_2) - \omega(P_1)$ is illustrated in figure 3. The solid and dotted curves represent two possible surface deformation waves of nearly the same wavelength $\lambda \simeq 2\pi/q_x \simeq 2a$. Since bending energy is proportional to curvature squared, the mode represented by the solid curve will have higher energy and frequency since $D_2 > D_1$. Another mode of nearly the same wavelength (dotted line) exists at a lower frequency. These two configurations correspond to P_2(solid) and P_1(dotted) respectively. Although there is an infinite series of gaps in the k_x-direction, $\omega(0, q_y)$ increases indefinitely along q_y. Thus, for any real ω, propagating modes in some direction (with a q_y component) can be found and complete (i.e. in all directions) band gaps do not exist. Also note that the gaps can increase at higher frequencies, e.g. $\omega(P_6) - \omega(P_5) > \omega(P_4) - \omega(P_3) > \omega(P_2) - \omega(P_1)$. This behaviour is not seen in typical periodic acoustic or electromagnetic dispersion relations, and is a consequence of the $\nabla_\perp^2(D(\boldsymbol{r})\nabla_\perp^2)$ term in the surface operator $\mathbf{L}(\boldsymbol{r}, \omega)$ which enhances the influence of variations in $D(\boldsymbol{r})$ at higher wavevectors. Waves with wavevectors near band gaps are standing because their group velocities $c_g = \partial_{\boldsymbol{q}}\omega(\boldsymbol{q}) \to 0$ as a Bragg plane ($q_x = (0, \pi)$, $q_y = 0$) is approached due to the inherent $\boldsymbol{q} \leftrightarrow -\boldsymbol{q}$ symmetry of $\omega(\boldsymbol{q})$. The sensitivity to D_1 is also shown in greater detail in figure 4(a); as D_1 increases the dispersion relation develops more of an upward curvature shown in figure 4(b) indicative of the increasing bending wave characteristics, due to the overall increase in surface bending rigidity. The gap widths may also increase with decreasing surface contrast $|D_1 - D_2|$ (cf. dotted *vs.* solid curves in figure 4(a)). This origin of this behaviour is the higher-order gradients acting on $D(\boldsymbol{r})$ in the dynamical boundary condition (2.8), and is absent in the periodic photonic, acoustic, and electronic problems.

Figure 5 shows the positions and widths of the first three band gaps (labelled ℓ corresponding to $\omega(P_{\ell+1}) - \omega(P_\ell)$) as a function of depth h for filling fraction $f = 0.8$, $D_1 = 0$ and $D_2 = 3.0$. Wave motions reach a depth of $\sim |k|^{-1}$, thus depth effects become important only when $|\boldsymbol{k}|h \lesssim 1$ such that the impenetrable bottom begins to influence the dispersion (2.9). Therefore, the higher-order band gaps (higher $|\boldsymbol{k}|$) saturate to their $h \to \infty$ limits at smaller depths.

Band gaps are sensitive to both filling fraction f and D_1. Figures 6(a) and 6(b) show the filling fraction dependence of the first three gaps for $D_2 = 3.0$, $h = \infty$, and $D_1 = 0$ and 1.0, respectively. Band gap widths are not monotonic functions of f and generally increase near larger values of f when $D_2 > D_1 \sim 0$. As expected, the gap frequencies are generally larger for smaller f when $D_1 > D_2$ (not shown). All gaps disappear at $f = 0$ and $f = 1$ as the interface becomes uniform. Note that for the second (and higher) bands, the gap widths alternate and disappear for special values of f. This property is a consequence of the alternating behaviour of $D(\boldsymbol{G})$. Higher bands have qualitatively similar behaviour but are at much higher frequencies, beyond the scale of figure 6.

The variation in band gaps as a function of D_1 is also analysed. The first, second, and third gaps as functions of D_1/D_2 ($D_2 = 3.0$) for $h = \infty$ and $f = 0.6$ and $f = 0.8$ are plotted in figures 7(a), 7(b) and 7(c), respectively. The first gap, shown in figure 7(a) is most sensitive to variations in D_1 near $D_1 = 0$. The gap increases rapidly from a small constant value as D_1 is increased until it vanishes as D_1 approaches D_2, when the surface becomes uniform. At this point the dispersion relation is governed by (2.9) in all directions. Figures 7(b) and 7(c) however, show special values of $D_1 \neq D_2$ where

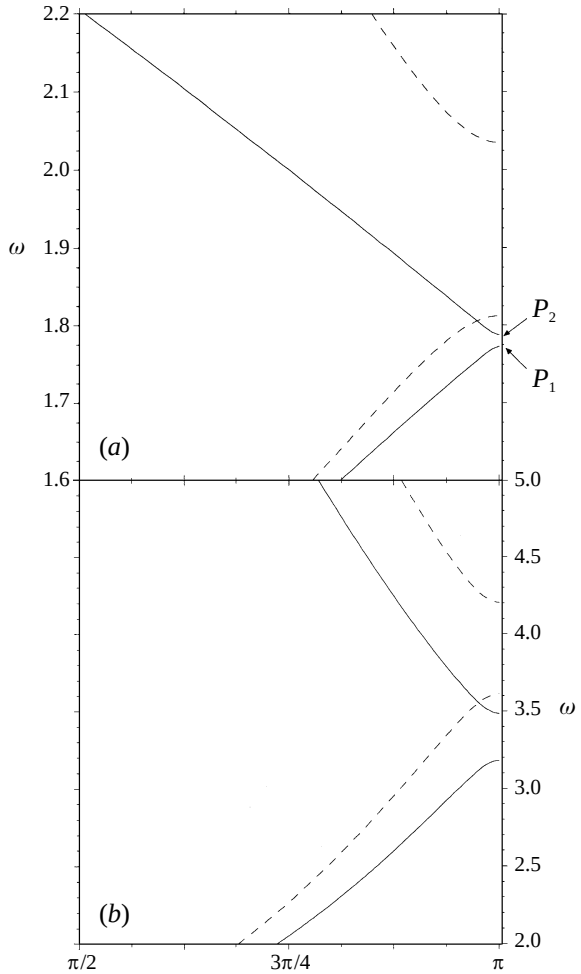

FIGURE 4. An expanded plot of the first band gap for $D_2 = 3.0$ and various D_1. (*a*) Solid curves, $D_1 = 0$ (P_1, P_2 labelled as in 2); dashed curves, $D_1 = 0.03$. The repeated zone notation is indicated. (*b*) Solid curves, $D_1 = 2.0$; dashed curves, $D_1 = 6.0$

the second and higher gaps vanish, similar to the vanishing of gaps as a function of f shown in figure 6.

3.2. *Two-dimensional periodicity*

We consider surface wave propagation through a periodic field of circular scatterers arranged in a two-dimensional lattice as shown in figure 1(*b*). The single scattering analogue has been considered in the context of wave scattering from a circular ice floe (Meylan & Squire 1996), or a circular patch of surfactant (Chou, Lucas & Stone 1995). The two-dimensional dispersion relations depend in a more complicated way on the direction of $\boldsymbol{q}$. We show the results for square and triangular lattices, where $|\boldsymbol{G}(0,1)| = |\boldsymbol{G}(1,0)| = 2\pi/a$ and $R_0 = a(f/\pi)^{1/2}$ for square lattices, and $|\boldsymbol{G}(0,1)| = |\boldsymbol{G}(1,0)| = 4\pi/\sqrt{3}a$ and $R_0 = 3^{1/4}a(f/2\pi)^{1/2}$ for triangular lattices. In the two-dimensional plots, we have chosen $D_2 = 100.0$ and $D_1 = 0$, corresponding to $d \sim 2.6$ cm of ice when $a = 100$ cm. We arbitrarily used $f = 0.3$ for the square lattice and

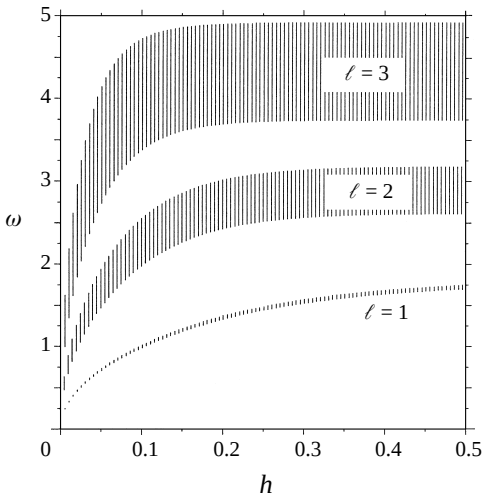

FIGURE 5. The first three band gaps at $(q_x, q_y) = (\pi, 0)$ as a function of water depth for $D_1 = 0$, $D_2 = 3.0$, $f = 0.8$. The height of the hatched regions labelled $\ell = 1, 2, 3$ correspond to $\omega(P_2) - \omega(P_1)$, $\omega(P_4) - \omega(P_3)$ and $\omega(P_6) - \omega(P_5)$, respectively.

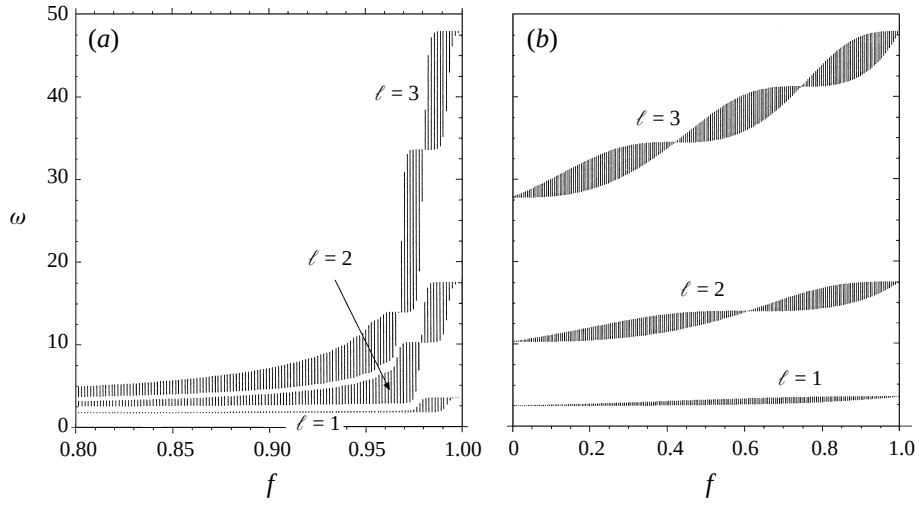

FIGURE 6. The first three band gaps as a function of filling fraction $f = w/a$ for (*a*) $D_1 = 0$ and (*b*) $D_1 = 1$, all other parameters are those of figure 5.

$f = 0.4$ for the triangular lattice. Note that the maximum filling corresponding to close packing is $f = \pi/4$ and $\pi/2\sqrt{3}$ for the square and triangular lattices respectively. The dispersion relations shown in figure 8 may qualitatively represent monochromatic wave propagation through pancake ice zones.

The first lowest eigenvalues (ω) for waves propagating over square and triangular lattices are plotted with $\boldsymbol{q}$ along the paths in the first two-dimensional BZ depicted below each plot in figure 8. The dashed curve corresponds to wave propagation over a uniform flexural rigidity of $\bar{D}$ in the repeated-zone scheme. The representative high symmetry points in wavevector space equivalent to $\boldsymbol{q} = 0, \boldsymbol{G}(1,0)/2$, and $(\boldsymbol{G}(1,0) + \boldsymbol{G}(0,1))/2$ are labelled Γ, X and M, respectively. The qualitative features depicted

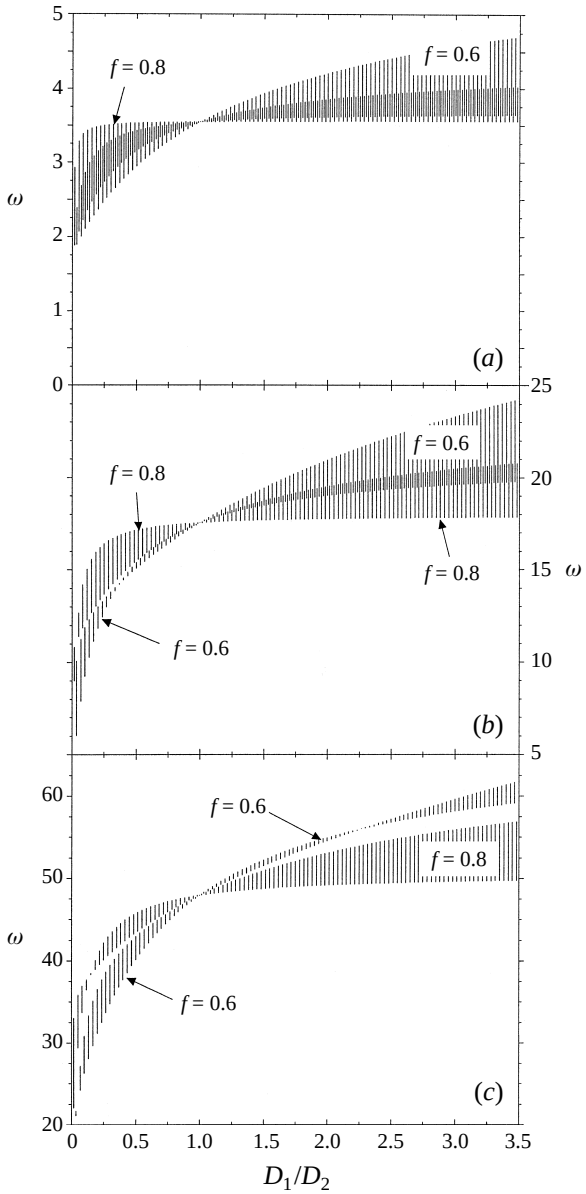

FIGURE 7. The first three band gaps, (*a*), (*b*), and (*c*), respectively as a function of bending rigidity mismatch D_1/D_2 at infinite depth and filling fractions $f = 0.6$ and 0.8.

in figure 8 are not as sensitive to the parameters as the one-dimensional periodicity considered above, although variations in band gap widths as functions of f and D_1/D_2 also occur at the Bragg points X and M. Due to the two-dimensional nature, the dispersion relation is highly degenerate along the plotted symmetry directions, and is usually made more apparent by plotting $\omega(\boldsymbol{k})$ along a specific direction. However, the main result displayed by figure 8 is that the gaps at Γ, X and M do not overlap each other in frequency, i.e. certain directions will always support propagating waves.

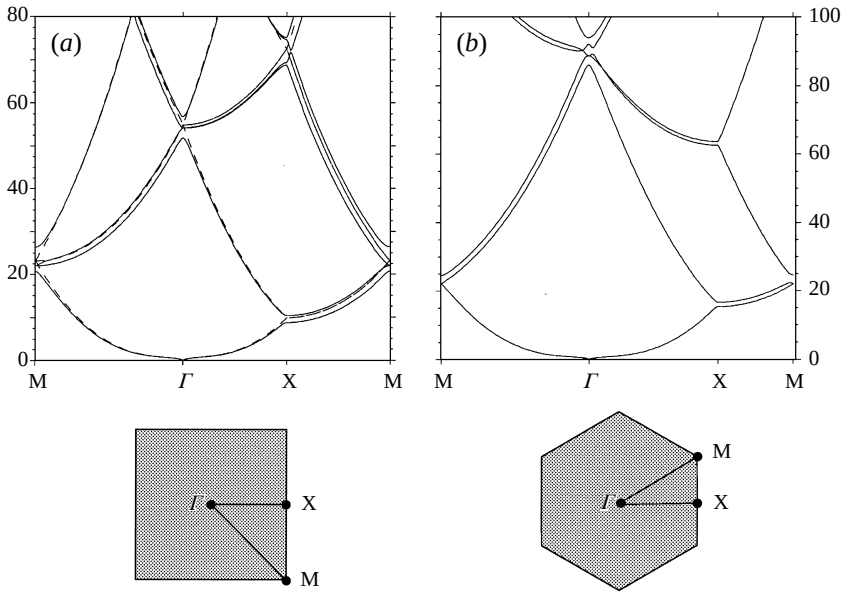

FIGURE 8. Two-dimensional infinite depth band structure for (*a*) square and (*b*) triangular lattice of circular plates of radius R_0. $D_2 = 100.0$, $D_1 = 0$. The filling fractions f used are 0.3 in (*a*) and 0.4 in (*b*). The first BZ in Fourier space (where $\boldsymbol{q}$ is restricted to the shaded regions) is depicted below each plot, with standard symmetry points labelled.

3.3. *Complete gaps; shallow water waves*

After a modest parameter search in f, D_1, D_2 and h, we find no complete low-order band gaps in two dimensions: there are always certain directions in which waves can propagate. This property is in contrast to photonic and phononic band structure, where complete gaps have been found by Joannopoulos *et al.* (1995), Kushwaha *et al.* (1993) and Sigalas & Economu (1992). The difference lies in the nature of the wave scattering and the boundary conditions at the scatterer edges. Firstly, the dispersion caused by wave impedance mismatch due to variations in D is weak, i.e. since $\omega^2 \simeq D_i q^5$, D_i must change by a considerable amount for the wavelengths $2\pi/q$ that would be excited in an infinite domain of uniform D_i to change appreciably at any given ω. Secondly, although higher derivatives $\eta(\boldsymbol{r}, t)$ are required to be discontinuous, the lower derivatives are continuous which limits the reflection from an edge discontinuity in D. Thus, scattering is not particularly strong in this system. Furthermore, the evanescent modes can couple the scatterers at high filling fractions. This is a direct analogy to total internal reflection of light by a prism. Bringing another prism close enough to the external surface captures the evanescent electromagnetic wave and couples the light wave out of the original prism. In the water scattering problem, these evanescent modes decay exponentially away from a surface scatterer with a length scale set by the depth, except in the $h \to \infty$ limit where they decay as a power law. Thus, evanescent modes in deep water can be important in effectively coupling the surface scatterings and prevent wave localization and complete band gaps. Since the gap widths in any direction tend to increase at higher bands, one might expect that complete gaps can be found at higher frequencies (or energies); however, this is not likely either since the dispersion relations and the positions of the gaps are very sensitive to $|\boldsymbol{k}|$ at high frequencies, and the chance that gaps in all directions overlap each other is small.

An interesting correspondence exists for gravity waves (uniform interface) in the presence of periodic bottom scatterers. The shallow water depth-averaged equation

$$\partial_t^2 \eta(\boldsymbol{r}) = g \nabla_\perp \cdot (h(\boldsymbol{r}) \nabla_\perp) \eta(\boldsymbol{r}) \tag{3.1}$$

is isomorphic to the acoustic wave equations in a fluid (no shear modulus). However, although complete acoustic band gaps have been found in square lattice geometries by Sigalas & Economu (1992), (3.1) actually corresponds to uniform compressive moduli, but different material densities in the fluid acoustic scattering context. In other words, the speed of sound and the density difference are constrained such that $(c_1/c_2)^2 = \rho_2/\rho_1$ for the analogy with (3.1) to hold. Under these conditions, Sigalas & Economu (1992) find no complete band gaps. Therefore, we conclude that the periodic-bottom shallow water wave problem has no complete band gaps.

4. Summary and conclusions

In this paper, we have presented a simple way of analysing the dispersion relation for surface flexural–gravity waves in the presence of periodic flexible surface scatterers. A generalization of Bloch's Theorem in a system with periodic boundary operators is established. The method is adapted from established techniques found in Ashcroft & Mermin (1976), Joannopoulos *et al.* (1995), and Sigalas & Economu (1992) for calculating multiple scattering in electronic, optical, and acoustic phenomena. Figures 2–8 encapsulate the main conclusions. The exact numerical calculations implicitly included all evanescent modes. We have treated the most computationally difficult case, that of sharp surface discontinuities, and conclude: (i) band gaps can exist in flexural surface scattering of monochromatic waves; (ii) the band gaps can increase with excitation frequency ω, at higher order; (iii) the sensitivity to depth is weak for $k_x h \gtrsim 0.5$ (1D); (iv) the sensitivity to f and D_1/D_2 can be strong; (v) certain special values of f and D_1/D_2 have vanishing gaps and (vi) the high dispersion in this system prevents the formation of complete band gaps in the two-dimensional case. The gaps discussed here are associated with non-propagating waves and correspond to the 'fully resonant' scattering from a finite number of periodic bottom undulations discussed in Davies *et al.* (1989) where their analyses broke down. Further exploiting the acoustic analogy, we also conclude that complete band gaps do not appear in periodic-bottom shallow water wave scattering.

Our description of band gaps, frequencies where water waves cease to propagate, implies possible structures for wave damping applications such as breakwaters. Within a large field of periodically spaced flexible plates, the band gaps determine the standing wave response, and reflect all travelling waves from the large field of plates. If a structure embedded in this field is susceptible to lateral wave forces, then it may be desirable to have large band gaps where waves are standing. Periodic surface scatterers can also function as wave frequency filters. The important result (v) above suggests that band gaps are generally not monotonic in f and D_2/D_1 and there are special values of these parameters which can be targeted or avoided depending on the application. Although it appears that no simple complete gaps exist for periodically bottom or surface scattered waves (due to a large dispersion in the surface scattering case, and due to uniform gravity in the shallow bottom scattering case), by appropriately choosing the two-dimensional surface periodicity relative to mean wind directions say, one may nonetheless shunt propagating waves for desired band gap frequencies. The effects of directionality of externally impinging

and internally generated waves can be inferred from the dispersion relations plotted in figures 2 and 8. More complicated structures where the basic unit cell of periodicity contains more that one scatterer can be treated by similar methods as described in this paper and elsewhere (Ashcroft & Mermin 1976 and Joannopoulos *et al.* 1995).

We have quantitatively treated only an infinite (periodic boundary condition) perfectly periodic array of scatterers. However, in real physical situations, boundaries and defects exist. For example, waves generated in the open ocean may impinge on a field of periodic scatterers, or defects may exist within a large array. Wave-induced lateral motions of the scatterers will cause deviations from perfect periodicity only at higher order in η, and exactly vanish at the band gaps where only standing waves are excited. Finally, this study suggests possible applications of other mathematical methods, traditionally used in studying wave and energy propagation in random systems, to study waves in Marginal Ice Zones (MIZ) (Wadhams *et al.* 1988), finite-sized systems, and surface waveguides and channels. It may be feasible to break ice in certain patterns to channel surface water wave energy much like optical waveguides (Joannopoulos *et al.* 1995). Defects in surface periodicity and interfacial disorder may also lead to evanescent modes and wave localization.

The author thanks T. J. Pedley for bringing to his attention the work of D. V. Evans, M. C. Payne for helpful discussions, M. G. Worster for comments on the manuscript, and D. Laurie for checking the numerical code.

Appendix. Discrete translational invariance and Bloch functions

We verify Bloch's Theorem for a velocity potential whose dynamics are governed by a periodic *boundary condition* operator $\mathbf{L}(\boldsymbol{r},\omega)$. The following derivation is an adaptation of that given for Schrödinger's equation in Chapter 8 of Ashcroft & Mermin (1976). Here, the equation satisfied by the bulk velocity potential $\nabla^2\varphi(\boldsymbol{r},z)=0$ is independent of $\boldsymbol{r},z<0$, although

$$\mathbf{L}(\boldsymbol{r},\omega)\equiv\lim_{z\to 0}\left[\rho g-\nabla_\perp\cdot(\sigma(\boldsymbol{r})\nabla_\perp)+\nabla_\perp^2(D(\boldsymbol{r})\nabla_\perp^2)\right]\partial_z \tag{A 1}$$

is invariant under discrete translations $\boldsymbol{r}\to\boldsymbol{r}+\boldsymbol{R}$, where $\boldsymbol{R}=n_i\boldsymbol{a}_i$ is any vector of the periodic lattice. Consider the translation operator $\mathbf{T}_{\boldsymbol{R}}$ such that

$$\begin{aligned}\mathbf{T}_{\boldsymbol{R}}\mathbf{L}(\boldsymbol{r},\omega)\varphi(\boldsymbol{r},z)&=\mathbf{L}(\boldsymbol{r}+\boldsymbol{R},\omega)\varphi(\boldsymbol{r}+\boldsymbol{R},z)\\&=\mathbf{L}(\boldsymbol{r},\omega)\mathbf{T}_{\boldsymbol{R}}\varphi(\boldsymbol{r},z)=(\mathbf{T}_{\boldsymbol{R}}\mathbf{L}(\boldsymbol{r},\omega))\varphi(\boldsymbol{r},z).\end{aligned} \tag{A 2}$$

Since the operators $\mathbf{T}_{\boldsymbol{R}}$ and $\mathbf{L}(\boldsymbol{r},z,\omega)$ commute in the function space defined by $\varphi(\boldsymbol{r},z)$, each is diagonal in this basis, i.e.

$$\mathbf{T}_{\boldsymbol{R}}\varphi\equiv c(\boldsymbol{R})\varphi,\quad \mathbf{L}(\boldsymbol{r})\varphi\equiv\rho\omega^2\varphi. \tag{A 3}$$

Note that any sum of lattice vectors yields another, $\boldsymbol{R}+\boldsymbol{R}'=\boldsymbol{R}''$. Therefore, applying $\mathbf{T}_{\boldsymbol{R}'}$ to the first of (A 3), and using the fact that two successive translations (by $\boldsymbol{R}$ and $\boldsymbol{R}'$) is equivalent to one by $\boldsymbol{R}''$,

$$\mathbf{T}_{\boldsymbol{R}}\mathbf{T}_{\boldsymbol{R}'}\varphi=c(\boldsymbol{R})c(\boldsymbol{R}')\varphi=\mathbf{T}_{\boldsymbol{R}+\boldsymbol{R}'}\varphi=c(\boldsymbol{R}+\boldsymbol{R}')\varphi. \tag{A 4}$$

A bounded solution to the constraint $c(\boldsymbol{R})c(\boldsymbol{R}')=c(\boldsymbol{R}+\boldsymbol{R}')$ is given by $c(\boldsymbol{R})=\mathrm{e}^{\mathrm{i}\boldsymbol{q}\cdot\boldsymbol{R}}$. Thus, $\varphi(\boldsymbol{r}+\boldsymbol{R},z)=\mathrm{e}^{\mathrm{i}\boldsymbol{q}\cdot\boldsymbol{R}}\varphi(\boldsymbol{r},z)$. Upon defining $\phi_{\boldsymbol{q}}(\boldsymbol{r},z)\equiv\mathrm{e}^{\mathrm{i}\boldsymbol{q}\cdot\boldsymbol{r}}\varphi(\boldsymbol{r},z)$, we find $\phi_{\boldsymbol{q}}(\boldsymbol{r},z)$ is periodic in $\boldsymbol{R}$, verifying (2.15).

REFERENCES

Andelman, D. Brochard, F. & Joanny, J.-F. 1987 Phase transitions in Langmuir monolayers of polar molecules. *J. Chem. Phys.* **86**, 3673–3681.

Ashcroft, N. W. & Mermin, N. D. 1976 *Solid State Physics*. W. B. Saunders, Philadelphia.

Belzons, M., Guazzelli, E. & Parodi, O. 1988 Gravity waves on a rough bottom: experimental evidence of one-dimensional localization, *J. Fluid Mech.* **186**, 539–558.

Black, J. L., Mei, C. C. & Bray, M. C. G. 1971 Radiation and scattering of water waves by rigid bodies. *J. Fluid. Mech.* **46**, 151–164.

Chou, T., Lucas, S. K. & Stone, H. A. 1995 Capillary wave scattering from a surfactant domain. *Phys. Fluids* **7**, 1872–1885.

Chou, T. & Nelson, D. R. 1994 Surface wave scattering at nonuniform interfaces. *J. Chem. Phys.* **101**, 9022–9032.

Davies, A. G., Guazzelli, E. & Belzons, M. 1989 The propagation of long waves over an undulating bed. *Phys. Fluids* A **1**, 1331–1340.

Devillard, P., Dunlop, F. & Souillard, B. 1988 Localization of gravity waves on a channel with a random bottom. *J. Fluid Mech.* **186**, 521–538.

Elter, J. F. & Molyneaux, J. E. 1972 The long-distance propagation of shallow water waves over an ocean of random depth. *J. Fluid Mech.* **53**, 1–15.

Fernyhough, M. & Evans, D. V. 1995 Scattering by a periodic array of rectangular blocks. *J. Fluid Mech.* **305**, 263–279.

Fox, C. & Squire, V. A. 1990 Reflection and transmission characteristics at the edge of shore fast ice. *J. Geophys. Res.* **95**, 11629–11639.

Gou, S., Messiter, A. F. & Schultz, W. W. 1993 Capillary-gravity waves in a surface tensoin gradient. I: Discontinuous change. *Phys. Fluids* A **5**, 966–972.

Heins, A. E. 1956 The scope and limitations of the method of Wiener and Hopf. *Commun. Pure Appl. Maths* **9**, 447–466.

Joannopoulos, J. D., Meade, R. D. & Winn, J. 1995 *Photonic Crystals: Molding the flow of Light*. Princeton University Press.

Kagemoto, H. & Yue, D. 1986 Interactions among multiple three-dimensional bodies in water waves: an exact algebraic method. *J. Fluid Mech.* **166**, 189–209.

Kirby, J. T. 1986 Current effects on resonant reflection of the surface water waves by sand bars. *J. Fluid Mech.* **186**, 501–520.

Kleinert, P. 1990 A field-theoretic treatment of third-sound localization. *Phys. Statist. Sol.* B **168**, 539–550.

Knobler, C. M. & Desai, R. C. 1992 Phase transitions in monolayers. *Ann. Rev. Phys. Chem.* **43**, 207–236.

Kushwaha, M. S., Halveli, P., Dobrzynski, L. & Djafari-Rouhani, B. 1993 Acoustic band structure of periodic composites. *Phys. Rev. Lett.* **71**, 2022–2025.

Liu, A. K. & Mollo-Christensen, E. 1988 Wave propagation in a solid ice pack. *J. Phys. Oceanogr.* **18**, 1702–1712.

Lucassen-Reynders, E. H. & Lucassen, J. 1969 Properties of capillary waves. *Adv. Coll. Interface Sci.* **126**, 154.

Mathews, J. & Walker, R. L. 1970 *Mathematical Methods of Physics*, 2nd Edn. Benjamin/Cummings Publishers.

McCall, S. L., Platzmann, P. M., Dalichaouch, R., Smith, D. & Schultz, S. 1991 Microwave propagation in two-dimensional dielectric lattices. *Phys. Rev. Lett.* **67**, 2017–2020.

Mei, C. C. 1983 *The Applied Dynamics of Surface Ocean Waves*. Wiley.

Mei, C. C. 1985 Resonant reflection of surface water waves by periodic sandbars. *J. Fluid Mech.* **152**, 315–335.

Mei, C. C., Hara, T. & Naciri, M. 1988 Note on the Bragg scattering of water waves by parallel bars on the seabed. *J. Fluid Mech.* **16**, 147–162.

Meylan, M. & Squire, V. A. 1994 The response of ice floes to ocean waves. *J. Geophys. Res.* **99**, 891–900.

Meylan, M. H. & Squire, V. A. 1996 Response of a circular ice floe to ocean waves. *J. Geophys. Res.* **101**, 8869–8884.

Mitra. A. & Greenberg, M. D. 1984 Slow interactions of gravity waves and a corrugated sea bed. *J. Appl. Mech.* **51**, 251–255.

Naciri, M. & Mei, C. C. 1988 Bragg scattering of water waves by a doubly periodic seabed. *J. Fluid Mech.* **192**, 51–74.

Porter, R. & Evans, D. V. 1995 Wave scattering by periodic arrays of breakwaters. *Wave Motion* **23**, 95–120.

Press, W. H., Teukolsky, S. A., Vetterling, W. T. & Flannery, B. P. 1992 *Numerical Recipes*. Cambridge University Press.

Sigalas, M. M. & Economou, E. N. 1992 Elastic and acoustic wave band structure. *J. Sound Vib.* **158**, 377–382.

Squire, V. A., Dugan, J. P., Wadhams, P., Rottier, P. J. & Liu, A. K. 1995 Of ocean waves and sea ice. *Ann. Rev. Fluid Mech.* **27**, 115–168.

Wadhams, P., Squire, V. A., Goodman, D. J., Cowan, A. M. & Moore, S. C. 1988 The attenuation rates of ocean waves in the marginal ice zone. *J. Geophys. Res.* **93**, 6799–6818.